

1 <https://doi.org/10.1016/j.enggeo.2021.106087>

2 THE ROLE OF INTERFACES IN THE BENTONITE BARRIER OF A NUCLEAR WASTE REPOSITORY ON
3 GAS TRANSPORT

4 María Victoria Villar^a, Beatriz Carbonell, Pedro Luis Martín, Carlos Gutiérrez-Álvarez

5 Centro de Investigaciones Energéticas, Medioambientales y Tecnológicas (CIEMAT), Avd.

6 Complutense 40, 28040 Madrid, Spain

7 ^acorresponding author: mv.villar@ciemat.es, +34 913466391

8

9 **Abstract:**

10 The FEBEX in situ test provided bentonite samples that had been submitted to the conditions
11 of the engineered barrier of a nuclear waste repository for 18 years. These samples can be
12 considered quite evolved from the microstructural point of view (aged, matured) when
13 compared with samples prepared in the laboratory under shorter and more usual time scales.
14 The barrier, composed of bentonite blocks, was hydrated with granitic groundwater under
15 natural conditions while it was submitted to the thermal gradient generated by a heater
16 mimicking the waste canister. Some of the samples were drilled between two bentonite
17 blocks, therefore they were crossed along by an interface. The gas permeability of samples
18 with and without interface was tested in the laboratory under different triaxial boundary
19 conditions.

20 Samples with an interface drilled in the inner part of the barrier (i.e. closer to the heater and
21 consequently drier) had higher gas permeability than samples of similar accessible void ratio
22 (related to dry density and water content) with no interface, and it was necessary to apply
23 higher confining pressures to reduce or suppress gas flow in them. Both observations point to

24 the interface as a preferential pathway for gas flow in this kind of samples. In contrast, wetter
25 samples drilled along interfaces of the external part of the barrier (which had very low
26 accessible void ratio, because of the high saturation), had permeabilities similar to those
27 corresponding to the same accessible void ratio in the reference, untreated bentonite. This
28 would prove the healing of the interfaces between blocks as a result of full saturation. The
29 importance of the testing boundary conditions, particularly with respect to confinement, on
30 gas transport processes was also highlighted.

31 **Keywords:** bentonite, gas transport, engineered barrier, saturation, porosity

32 **1 Introduction**

33 Geological disposal is the preferred, internationally accepted option for wastes with high levels
34 of radioactivity. The safety of the concept relies on a series of barriers, both engineered and
35 natural, between the waste and the surface acting in concert to contain the wastes. Bentonites
36 or bentonite-based materials have frequently been proposed to construct the engineered
37 barrier around the waste container (buffer) because of their high retention capacity, high
38 swelling ability and low permeability.

39 The heat released by the waste will induce a thermal gradient through the bentonite barrier,
40 while groundwater will tend to flow into it. As a consequence, coupled thermal, hydraulic,
41 mechanical and geochemical processes will take place during the transient period of the
42 repository life. In advance stages of the repository gas will be generated by several
43 mechanisms, such as the anaerobic corrosion of metals, the microbial degradation of organic
44 wastes and the radiolysis of water, which generate hydrogen, oxygen, methane and carbon
45 dioxide. The gas generated can dissolve in the pore water according to Henry's law and move
46 away with it, but if the volume of gas generated is too large, a separate gas phase would exist
47 in the bentonite barrier (e.g. Ortiz et al. 2002). The transport of this gas phase would involve

48 both visco-capillary two-phase flow under low pressure (without significant deformation of the
49 pore space) and microscopic pathway dilation, depending on the degree of saturation of the
50 bentonite, i.e. on the gas accessible void ratio (Olivella and Alonso 2008, Sellin and Leupin
51 2013, Villar et al. 2013, Graham et al. 2016). If the generation rates are higher than the rate by
52 which gas is transported away within the repository, the gas pressure could rise and build up,
53 but gas migration would not occur unless the applied gas pressure exceeded the total stress
54 experienced by the clay (resulting from the sum of the water pressure and the swelling
55 pressure), i.e. until the *breakthrough* value was reached (Horseman et al., 1999; Harrington
56 and Horseman, 2003). As a result, a mechanical interaction between the gas and clay will
57 begin, leading to the generation of gas pathways, which might affect the barrier properties and
58 drive contaminated water into the geosphere. Thus, the knowledge of the movement of gases
59 through the repository structure is required to determine the magnitude of these effects and
60 to accommodate them in the repository design and safety calculations.

61 In the context of studies related to the geological disposal of radioactive waste, and with a
62 focus on the engineered barrier performance, the FEBEX in situ test was the first real scale test
63 of a horizontal disposal system for high-level radioactive waste, performed under natural
64 conditions in crystalline rock (ENRESA 2006). A gallery of 2.3 m in diameter was excavated
65 through the granite at the Grimsel Test Site (Switzerland) and two heaters, that simulated the
66 thermal effect of the wastes, were placed concentrically, surrounded by a barrier of highly-
67 compacted bentonite blocks. The external surface temperature of the heaters was 100°C and
68 the bentonite was slowly hydrated by the granitic groundwater. After 5 years of operation, half
69 of the installation was dismantled, and the other half continued in operation with just one
70 heater under the configuration shown in Fig. 1. In 2015, after 18 years operation, the FEBEX
71 Dismantling Project (FEBEX-DP) undertook the dismantling of the remaining half of the
72 experiment (García-Siñeriz et al. 2016).

73 The bentonite engineered barrier of the FEBEX in situ test was composed of compacted blocks
74 among which there were interfaces (Fig. 2). The blocks were manufactured in the shape of
75 12-cm thick circular crown sectors and arranged in vertical slices consisting of concentric rings.
76 The blocks were obtained by uniaxial compaction of the FEBEX clay with its hygroscopic water
77 content applying pressures of between 40 and 45 MPa, what caused dry densities of 1.69-1.70
78 g/cm³. The initial dry density of the blocks was selected by taking into account the probable
79 volume of the construction gaps and the need to have a barrier with an average dry density of
80 1.60 g/cm³ (ENRESA 2006). The initial aspect of some of these construction gaps can be seen
81 on the left-hand side of Fig. 2, whereas their appearance upon dismantling after 18 years
82 operation is shown on the right-hand side. The hydration and swelling of the bentonite caused
83 the closing and sealing of all the gaps, both those among blocks of the same slice and the gaps
84 between adjacent bentonite slices that cannot be seen in this Figure. There was no effect of
85 the vertical gaps between bentonite slices on the water content and dry density distribution,
86 which proves that they were not preferential water pathways (Villar et al. 2016, 2020a). The
87 same had already been observed during the partial dismantling, after five years of operation
88 (Villar et al. 2005). Fig. 1 shows the water content isolines of the barrier drawn from on-site
89 measurements performed during dismantling in 2015. The water content was higher than the
90 initial one in all locations, but decreased from the granite towards the heater, whereas the dry
91 density increased in the same sense (Villar et al. 2016, 2020a).

92 During dismantling numerous bentonite samples were taken and sent to different laboratories
93 for analysis. Some of the samples were obtained by drilling the bentonite surface exposed
94 when the previous bentonite slice was removed. The gas permeability of some of these core
95 samples was measured with the aim of checking:

- 96 – the influence on gas permeability of the physical state of the samples in terms of water
97 content and dry density and consequently of degree of saturation,

- 98 – the effect of the boundary conditions on gas permeability, namely gas injection pressure
- 99 and confining pressure,
- 100 – the change of gas transport properties with respect to the untreated, reference FEBEX
- 101 bentonite and
- 102 – the role of interfaces on gas transport.

103 To accomplish the last aim, the samples were drilled both in the middle of blocks and along the
104 interface between two blocks, as indicated in Fig. 2. Fig. 1 shows the sampling sections from
105 which the samples tested in this investigation were taken.

106 To the authors' knowledge, the research reported in this paper is the first systematic study on
107 the gas transport properties of bentonite samples submitted to repository-like conditions for a
108 long period of time, consequently of matured, aged bentonite. It is also the first experimental
109 investigation about the role on gas transport of interfaces between bentonite blocks of an
110 engineered barrier.

111 **2 Background: gas transport studies in FEBEX bentonite**

112 The research on the gas transport properties of FEBEX bentonite started back in the 90s, when
113 the gas permeability of samples compacted to different dry densities and water contents was
114 measured in a falling-head permeameter (described below in section 3.3.1), using very low
115 injection pressures (Villar and Lloret 2001, Villar 2002). Gas permeability was found to depend
116 on the accessible void ratio, which expresses the ratio between gas accessible volume (not
117 blocked by water) and particle volume. It is computed as $e(1-S_r)$, with e being the void ratio
118 and S_r the degree of saturation. It was also found that the intrinsic permeability deduced from
119 gas flow was considerably higher than that deduced from water flow, which was because of
120 the microstructural changes that take place during saturation, namely the reduction in average
121 pore size. Because of the equipment limitations, it was not possible to measure the gas

122 permeability of samples with high degrees of saturation. New setups were developed in the
123 framework of the European FORGE project (<https://www.bgs.ac.uk/forge/>), which allowed to
124 measure the permeability of samples with degrees of saturation up to 97% and test the effect
125 of confining pressure and gas injection and backpressures on the gas permeability value. In
126 these tests, the applied pressure gradient directly controlled the resulting gas flow rate,
127 attesting conventional visco-capillary flow. The new results also allowed to confirm the
128 potential relation between accessible void ratio and gas permeability, with exponents between
129 3 and 4. Furthermore, it was checked that the Klinkenberg effect was not significant for this
130 material in the range of pressure tested (Villar et al. 2013, Gutiérrez-Rodrigo 2018).

131 The tests mentioned in the previous paragraph were all performed in triaxial cells. But during
132 the FORGE project, tests were also performed on samples fully saturated inside stainless steel
133 cylindrical cells, where the overall volume of the bentonite could not change during the tests.
134 Those tests were designed to determine the gas breakthrough pressure and additionally
135 estimate a permeability value once breakthrough occurred (Villar et al. 2013, Gutiérrez-
136 Rodrigo et al. 2015, 2021; Gutiérrez-Rodrigo 2018). These permeability values were computed
137 assuming two-phase flow as gas transport mechanism for lack of a better approximation. The
138 gas breakthrough pressure values in saturated bentonite increased clearly with dry density,
139 and they were always higher than the swelling pressure of the bentonite. The permeabilities
140 computed after breakthrough seemed to be independent of the dry density (Gutiérrez-Rodrigo
141 et al. 2021).

142 The tests performed in the triaxial cells and in the stainless steel cells mentioned above were
143 designed to measure the bentonite gas permeability and the gas breakthrough pressure,
144 respectively. The combination of both types of results allowed to conclude that in compacted
145 bentonite two-phase flow can take place for degrees of saturation lower than about 97%,
146 whereas, for higher degrees of saturation, pathway dilation could be the predominant

147 mechanism after a given breakthrough pressure was reached. The stability of the pathways
148 would depend on the degree of saturation and dry density of the samples. For partially
149 saturated bentonite, the gas pathways seemed to be stable, since for a given pressure gradient
150 there was a stable flow. Nevertheless, the drop in effective gas permeability when approaching
151 full saturation is that of several orders of magnitude (Villar et al. 2013, Gutiérrez-Rodrigo et al.
152 2015), indicating an important restriction of the gas flow inside the bentonite. In almost
153 completely saturated samples of bentonite, in which it was necessary to apply a high pressure
154 to induce flow (breakthrough pressure), when the pressure gradient dropped below a given
155 value (residual pressure), flow stopped, which was interpreted as the closing of the pathways.

156 In the gas breakthrough tests, the role of an interface along the cylindrical specimen was
157 tested. To this aim, the cylindrical specimen obtained by uniaxial compaction was
158 longitudinally cut and the two halves obtained were put together in the stainless steel cell and
159 then saturated prior to breakthrough testing. The results indicated that a sealed interface
160 along a saturated bentonite specimen had no effect on the breakthrough pressure values
161 (Gutiérrez-Rodrigo et al. 2021).

162 The specimens used to perform the tests summarised above were obtained either by uniaxial
163 compaction of the granulated bentonite mixed with different quantities of deionised water
164 (tests in triaxial cells), or by compaction of the bentonite with its hygroscopic water content
165 that was subsequently saturated inside the testing cell (tests in isochoric stainless steel cells).
166 In the latter case the samples were saturated for periods of time that spanned from 2 to 28
167 months. In addition to these kinds of samples, specimens coming from the final dismantling of
168 the FEBEX in situ test were also tested for gas permeability in the triaxial cells. These samples
169 had been subjected to repository-like conditions for 18 years and were consequently quite
170 “mature” in terms of evolution of the microstructure, which is something that cannot be
171 reached in laboratory experiments. They were overall highly saturated, except for those taken

172 closer to the heater that simulated the waste container. Namely, samples with initial degrees
173 of saturation between 79 and 100% were tested. The results obtained were reported in Villar
174 et al. (2018a) and part of them published in Carbonell et al. (2019). The whole set of results is
175 summarised here, including those obtained in samples with interface.

176 **3 Material and methods**

177 **3.1 Material: the FEBEX bentonite**

178 The material used to construct the clay buffer of the FEBEX in situ test was the FEBEX
179 bentonite, extracted from the Cortijo de Archidona deposit (Almería, Spain). At the factory, the
180 clay was disaggregated and gently dried to a water content of around 14%, all the material of
181 particle size greater than 5 mm being rejected. The processed material was used for
182 fabrication of the blocks for the large-scale test and for the laboratory tests performed for the
183 characterization of the clay. The physico-chemical properties of the FEBEX bentonite, as well as
184 its most relevant thermo-hydro-mechanical and geochemical characteristics were reported in
185 ENRESA (2006) and updated in e.g. Villar (2017) and are summarised below.

186 The smectite content of the FEBEX bentonite is above 90 wt.%. The smectitic phases are
187 actually made up of a montmorillonite-illite mixed layer, with 10-15 wt.% of illite layers.
188 Besides, the bentonite contains variable quantities of quartz, plagioclase, K-felspar, calcite, and
189 cristobalite-trydimite. The cation exchange capacity is 98 ± 2 meq/100g, the main exchangeable
190 cations being calcium (35 ± 2 meq/100g), magnesium (31 ± 3 meq/100g) and sodium (27 ± 1
191 meq/100g). The predominant soluble ions are chloride, sulphate, bicarbonate and sodium.

192 The liquid limit of the bentonite is 102 ± 4 %, the plastic limit 53 ± 3 %, the density of the solid
193 particles 2.70 ± 0.04 g/cm³, and 67 ± 3 % of particles are smaller than 2 µm. The hygroscopic
194 water content in equilibrium with the laboratory atmosphere (relative humidity 50 ± 10 %,

195 temperature $21\pm 3^\circ\text{C}$) is $13.7\pm 1.3\%$. The external specific surface area is $32\pm 3\text{ m}^2/\text{g}$ and the
196 total specific surface area is about $725\pm 47\text{ m}^2/\text{g}$.

197 The saturated hydraulic conductivity of compacted samples of the FEBEX reference bentonite
198 is exponentially related to their dry density. The empirical relationship between intrinsic
199 permeability (k_{iw} , m/s) and dry density (ρ_d , g/cm^3) shown in Eq. 1 was obtained for samples
200 compacted to dry densities above $1.47\text{ g}/\text{cm}^3$ and permeated with deionised water at room
201 temperature (Villar 2002). According to this relationship, for a dry density of $1.6\text{ g}/\text{cm}^3$ the
202 intrinsic permeability of the bentonite is about $5\cdot 10^{-21}\text{ m}^2$.

$$203 \quad \log k_{iw} = -2.96 \rho_d - 15.57 \quad [1]$$

204 The swelling pressure (P_s , MPa) of compacted samples is also exponentially related to the
205 bentonite dry density, according to the empirical expression in Eq. 2 (Villar 2002), which
206 indicates that when the bentonite at dry density of $1.6\text{ g}/\text{cm}^3$ is saturated under constant
207 volume with deionised water at room temperature, the swelling pressure has a value of about
208 6 MPa:

$$209 \quad \ln P_s = 6.77 \rho_d - 9.07 \quad [2]$$

210 As mentioned in section 2, the gas effective permeability of samples of FEBEX bentonite
211 compacted to different dry densities with various water contents was measured under
212 confining pressures of 0.6 and 1.0 MPa (Villar 2002, Villar et al. 2013). The gas permeability
213 values obtained were related to the accessible void ratio through

$$214 \quad k_{ig} \cdot k_{rg} = 1.25 \cdot 10^{-12} (e(1 - S_r))^{3.22} \quad [3]$$

215 **3.2 Sample preparation**

216 The samples used were obtained by drilling the bentonite barrier of the FEBEX in situ test at
217 the Grimsel Test Site during dismantling (named hereafter FEBEX-DP samples). Half of the

218 samples were drilled in the middle of blocks and the other half at the contact between two
219 blocks, so that to have an interface along the core. The name of the samples was given as BC-
220 SS-n, where BC stands for “bentonite core”, SS indicates the section from which the sample
221 was drilled (S44, S47, S53, according to Fig. 1) and n is a consecutive number.

222 To prepare the samples in the laboratory, the core diameter was fit to that of the testing cells
223 (36 or 50 mm) by using a cutting ring and a knife and sand paper in some cases. The cylindrical
224 surface of the samples was smoothed and the parallelism of the cylinder’s ends was ensured.
225 The resulting specimens were between 2.4 and 5 cm in height and 10-20 cm² in surface area.
226 In some cases the interface along the core became distinct only after preparing the specimen
227 (Fig. 3). To determine the initial water content and dry density of the samples (and in some
228 cases the pore size distribution), a spare fragment resulting from the sample preparation was
229 used. The characteristics of the samples have been included in Table SM1 (in Supplementary
230 Material, available online). The initial water contents determined in these core samples were
231 similar, or slightly higher, than those determined in adjacent blocks, which were used to draw
232 the isolines plotted in Fig. 1 (also included in Table SM1 and compared in Fig. SM1). The
233 process of trimming could have caused certain external drying of the samples, as discussed
234 below in section 4.5.

235 Filter paper and porous stones were placed on top and bottom of the samples. The
236 assemblage thus prepared was laterally wrapped in double latex membranes or in EPDM
237 (ethylene propylene diene monomer) rubber over a latex membrane. Other samples were
238 wrapped in duct tape and finally in an EPDM rubber membrane. Vacuum grease was applied
239 between membranes in order to prevent the loss of gas. These assemblages were placed in
240 triaxial cells.

241 **3.3 Experimental setups**

242 The same sample was tested consecutively in two different setups without removing it from
243 the triaxial cell. The first setup, which worked as a low-pressure, falling-head permeameter,
244 had been used in the investigations with FEBEX bentonite initially reported in Villar and Lloret
245 (2001) and Villar (2002), where the setup was described in detail. Results obtained in this
246 setup for the reference, untreated bentonite were used to assess the changes in the gas
247 transport properties of the FEBEX-DP samples (see section 4.4). The second setup was a high-
248 pressure equipment that could either work as a falling-head (unsteady-state) or as a constant-
249 head (steady-state) permeameter. Under both configurations a variety of boundary conditions
250 was allowed (Villar et al. 2018a, Carbonell et al. 2019).

251 A total of 19 core samples were tested, eight of which were crossed by an interface. Only four
252 of them were not initially tested in the low-pressure equipment.

253 **3.3.1 Low-pressure equipment (LP)**

254 Once the triaxial cell was filled with water, a confining pressure high enough to ensure perfect
255 adherence of the membranes to the surface of the sample was applied to the chamber of the
256 triaxial cell. The inlet at the lower part of the sample was connected to an airtight tank of
257 known volume, in which nitrogen gas was injected at a pressure slightly higher than
258 atmospheric. The tank was instrumented with a pressure sensor connected to a data
259 acquisition system which recorded the pressure of the fluid contained inside. The inlet at the
260 upper end of the sample was left open to the atmosphere. The test consisted in allowing the
261 gas in the tank to go out to the atmosphere through the specimen, while the decrease in
262 pressure in the tank was measured as a function of time. A schematic design of this setup is
263 shown in Fig. SM2.

264 The effective permeability to gas ($k_{ig} \cdot k_{rg}$ [m^2], with k_{ig} being the intrinsic permeability measured
 265 with gas [m^2] and k_{rg} the relative permeability to gas) was calculated in accordance with the
 266 following equation (Yoshimi and Osterberg 1963):

$$267 \quad k_{ig} \cdot k_{rg} = 2.3 \times \frac{V \times L \times \mu_g}{A \times \left(P_{atm} + \frac{P_0}{4} \right)} \times \frac{-\text{Log}_{10} \left(\frac{P(t)}{P_0} \right)}{t - t_0} \quad [4]$$

268 where V is the volume of the tank (m^3), L is the length of the sample (m), A is the surface area
 269 of the sample (m^2), μ_g is the dynamic viscosity of nitrogen under the test conditions ($1.78 \cdot 10^{-5}$
 270 Pa·s), P_{atm} is atmospheric pressure (Pa), P_0 is the excess pressure over atmospheric pressure in
 271 time t_0 (s) and $P(t)$ is the excess over atmospheric pressure (Pa) in the tank at time t (s). This
 272 equation was developed in a way analogous to that used for the expression of permeability to
 273 water using a falling head permeameter, with the air continuity equation being applied
 274 through consideration of compressibility (Lloret 1982).

275 The volume of the spherical tank used, was $2.21 \cdot 10^{-2} m^3$ and the gas used for the tests was
 276 nitrogen, for which a density of $1.12 kg/m^3$ was taken. The tests were performed at room
 277 temperature ($22.6 \pm 1.3^\circ C$). Prior to every new permeability test, the airtightness of the system
 278 was checked.

279 Taking into account the cited values for the density and the viscosity of nitrogen, the following
 280 relation between permeability to gas (k_g , m/s) and the effective permeability in Eq. 4 is
 281 obtained:

$$282 \quad k_g = \frac{\rho_g \times g}{\mu_g} \times k_{ig} \cdot k_{rg} = 6.2 \cdot 10^5 \times k_{ig} \cdot k_{rg} \quad [5]$$

283 The triaxial cell was initially pressurised to 0.6 MPa. This confining pressure was chosen
 284 because it is well below the apparent preconsolidation stress of the samples and consequently

285 would not cause any significant sample deformation (swelling during the tests was not
286 expected because no additional water was provided to the samples). The pressure of the tank
287 on test initiation was fixed to values close to 103 kPa (relative pressure). The test continued
288 until the pressure decrease rate allowed to compute a constant permeability value or until the
289 pressure tank was emptied. In some of the samples no flow occurred under these pressure
290 conditions, but if flow took place, the confining pressure was increased to 1 MPa, and the test
291 was repeated, previously increasing again the gas tank pressure. Afterwards, the cell with the
292 sample was moved to the high-pressure equipment.

293 **3.3.2 High-pressure equipment (HP)**

294 Two different configurations of the high-pressure gas permeability setup were used for these
295 tests, which were performed in the same samples previously tested in the low pressure
296 equipment described above (Villar et al. 2018a). The first tests were performed in a setup in
297 which a small gas cylinder was connected to the upper end of the sample, the pressure in it
298 was initially fixed and allowed to decrease as flow took place through the sample, following
299 the working principle of an unsteady-state permeameter (HP-US). Only three samples were
300 tested under this configuration. Afterwards the setup was modified in order to improve the
301 accuracy of the results of the tests, and flowmeters were installed to measure gas outflow.
302 Under this configuration the tests were performed by keeping constant confining and injection
303 pressures and atmospheric backpressure, i.e. following the working principle of a steady-state
304 permeameter (HP-S).

305 The general testing protocol followed approximately these phases:

- 306 – Phase 1: the tests started under confining pressure of 0.6 or 1 MPa (depending on the last
307 confining pressure applied in the LP setup), injection pressure of 100 kPa and atmospheric
308 backpressure. If there was no flow or it was very low, the injection pressure was increased
309 in 100-kPa steps to cause larger flow.

- 310 – Phase 2: Once the flow was sufficiently high to be measured accurately or the difference
311 between confining and injection pressures was lower than 200 kPa (to ensure that gas flow
312 did not take place between the membrane and the sample external surface), the confining
313 pressure was progressively increased until gas could not flow through the sample.
- 314 – Phase 3: Finally, the confining pressure was stepwise decreased, keeping the injection
315 pressure constant.

316 The particular pressure values reached in each of these phases depended on the
317 characteristics of the samples. In those with high permeability, Phase 1 was very short (the
318 injection pressure did not have to be increased because flow was initially high) and the
319 confining pressure in Phase 2 had to be increased to very high values to stop flow. In contrast,
320 some samples with very low permeability could only be submitted to Phase 1, because flow
321 was too low to decrease it even further by increasing the confining pressure.

322 The duration of each step was nominally fixed to 24 hours, although when flow was high it had
323 to be shortened to avoid unnecessary drying of the samples or exhausting of the pressure
324 vessels.

325 *High-pressure, unsteady-state (HP-US)*

326 The general setup consisted of two stainless steel pressure cylinders connected to the inlets of
327 the triaxial cell and equipped with pressure sensors: an inlet transducer GE UNIK 5000 (350
328 bar-a, 0.04% FS BSL) and an outlet transmitter DRUCK PTX 1400 (100 bar-sg, 0.25% BSL max).
329 Vacuum was applied to the downstream cylinder (the one connected to the bottom of the
330 sample) and the other one was pressurised with nitrogen gas to 200 kPa. If no changes in
331 pressure were recorded for 24 h, the injection pressure was increased by 100 or 200 kPa. The
332 process was repeated until gas started to flow through the sample, causing a decrease of
333 pressure in the upstream cylinder and an increase in the downstream one. The confining

334 pressure was applied to the water in the triaxial cell with a pressure bladder accumulator or a
335 pressure/volume piston controller. A schematic design of the setup is shown in Fig. 4.

336 Instantaneous gas flow rates under the imposed pressure gradient, entering in or coming out
337 from the sample, could be calculated from the volume of the upstream/downstream cylinders
338 and the instantaneous rate of pressure change (Loosveldt et al. 2002), avoiding the need for a
339 flow-rate measuring device. Hence, the mean volume flow rate Q_m , where the subscript 'm'
340 refers to reference conditions of T and P under which the mass flow was measured, was
341 calculated as:

$$342 \quad Q_m = V_v \times \left(\frac{\Delta\rho}{\rho} \right) \times \frac{1}{\Delta t} \quad [6]$$

343 where V_v is the volume of the cylinder (150 or 300 cm³), $\Delta\rho/\rho$ is the relative change in gas
344 density, and Δt is the time interval in which the change in gas density took place.

345 Considering that the tests were isothermal, the following relation can be obtained (see
346 Gutiérrez-Rodrigo et al. 2015, Gutiérrez-Rodrigo 2018):

$$347 \quad Q_m = V_v \times \left(\frac{\Delta P}{P_{av}} \right) \times \frac{1}{\Delta t} \quad [7]$$

348 where V_v is the volume of the cylinder, ΔP is the pressure change and P_{av} is the average
349 pressure (upstream or downstream) in the cylinder (inlet or outlet) during the time interval
350 considered (Δt).

351 To compute the effective permeability ($k_{ig} \cdot k_{rg}$, m²) the gas inflow or outflow can be used,
352 applying the following equation for incompressible media with compressible pore fluids
353 (Scheidegger 1974):

$$354 \quad k_{ig} \cdot k_{rg} = \frac{Q_m \times \mu_g \times L \times 2 P_m}{A \times (P_{up}^2 - P_{dw}^2)} \quad [8]$$

355 where Q_m is the mean volume flow obtained applying Eq. 7, A , μ_g and L are the same as in
 356 previous equations and P_{up} and P_{dw} are the upstream and downstream pressures (kPa) applied
 357 at the top (inlet) and the bottom (outlet), respectively, of the sample. In this kind of tests the
 358 measurement pressure P_m and the average pressure of the interval P_{av} are the same.

359 The accuracy of this analysis depends on these assumptions: 1) the gas compressibility did not
 360 affect the volumetric flow (gas behaved as an ideal gas), and 2) a quasi-steady mass-flow state
 361 was established, *i.e.* the quantity of gas exiting the high pressure cylinder was approximately
 362 equal to that entering the low pressure cylinder, without accumulation of gas mass inside the
 363 sample over the time period of interest.

364 *High-pressure, steady-state (HP-S)*

365 In this setup the injection pressure could be independently varied and maintained constant
 366 during the period of time necessary to get steady flow, while the backpressure remained
 367 atmospheric and the outflow was measured. Outflow gas rates, upstream and downstream
 368 pressure, confining pressure and temperature were monitored online. The equipment was
 369 described in detail in Villar et al. (2018a) and Carbonell et al. (2019) and is shown in Fig. SM3.

370 The same gas injection lines as in the HP-US configuration were used, which allowed to apply
 371 injection pressures of up to 18 MPa. The outlet of the cell connected to the bottom of the
 372 sample was open to atmosphere, with a series of different range HITECH gas mass flowmeters
 373 (0.04-2, 0.2-10, and 2-100 STP cm³/min) measuring the gas outflow, the value used to compute
 374 permeability being the one measured by the flowmeter working in the proper range. To apply
 375 the confining pressure the same devices as in the HP-US equipment were used.

376 To compute the apparent (effective) permeability, the gas outflow measured was used in Eq.
377 8. In this kind of test, Q_m is the mean volume flow rate measured by the appropriate
378 flowmeter, P_m is the standard atmospheric pressure (101.325 kPa) due to the STP conditions of
379 the gas mass flowmeters and $(P_{up}^2 - P_{dw}^2)$ is the difference between the gas injection pressure
380 and the backpressure (actual atmospheric pressure in this setup).

381 **3.4 Final determinations**

382 At the end of the tests, the bentonite specimens were measured and weighed and the water
383 content and dry density at three different levels (two, if they were too short) along the
384 cylindrical specimens were determined. To determine the dry mass of the samples they were
385 oven-dried at 110°C for 48 h, and to compute the dry density, the volume of the same
386 specimens was determined by immersing them in mercury prior to drying and weighing the
387 fluid displaced.

388 The degrees of saturation (S_r) were computed from the dry density and water content
389 determined in the laboratory, taking a value for the water density of 1 g/cm³.

390 The pore size distribution was determined by mercury intrusion porosimetry (MIP). This
391 technique allows the determination of the pore size distribution by injecting mercury into the
392 sample at different pressures while controlling the volume intruded. The pressure applied may
393 be related to the minimum pore diameter intruded, taking into account the characteristics of
394 the fluid. The ratio of the volume of mercury intruded (pore volume) to the applied pressure
395 (which conditions the minimum pore diameter accessed) allows distribution curves to be
396 obtained establishing the percentage of pores of a size included within a given range.

397 Two pieces of each sample were used: a spare fragment resulting from the sample preparation
398 and a fragment from the sample at the end of the gas permeability test. To remove the water
399 of the samples prior to MIP testing they were lyophilised. The porosimeter used was a

400 Micromeritics AutoPore Series IV 9500, which allowed the exploration of pore diameters
401 between 0.006 and 600 μm .

402 **4 Results**

403 Nineteen gas permeability tests were performed in triaxial cells with bentonite samples
404 obtained by on-site drilling of the bentonite barrier. The dry density of the samples was
405 between 1.64 and 1.51 g/cm^3 and the water content between 29 and 19% (S_r between 79 and
406 104%). In each sampling section (Fig. 1) gas testing was carried out in samples taken at the
407 same distance from the gallery wall drilled in the middle of a block (sound samples) and
408 between two blocks (samples with interface). This way, at least six samples per section were
409 tested, two from each barrier ring (external, middle and inner, Fig. 2), half of which had an
410 interface along them. The comparison of the results obtained in both kinds of samples (with
411 and without interface) should allow to assess the role of the interface on gas transport. Some
412 of the results obtained in sound samples were presented in Carbonell et al. (2019), but are
413 given here again for completeness. Out of the samples tested, eight had been drilled between
414 two blocks and consequently had an interface along them. The characteristics of each sample
415 tested, the pressure path followed and the detailed results obtained were reported in Villar et
416 al. (2018a) and summarised in Tab. SM1. As an example, the results obtained in two of these
417 samples are described in detail in the following sections. Afterwards, specific aspects of the
418 results obtained in all the samples are discussed.

419 The samples were not artificially saturated prior to gas testing. Most samples were initially
420 tested in the low-pressure setup and then in the high-pressure setup, where the pressure
421 paths described in section 3.3.2 were approximately followed. The precise pressure paths
422 depended on the characteristics of the samples and consequently were quite heterogeneous.

423 When flow occurred under a given pressure situation, the duration of the steps was generally
424 short (1-2 hours). In many cases it was observed that, if the same pressure situation was kept
425 for longer, flow decreased and the permeabilities computed were lower. This aspect has not
426 been analysed in detail but could have some effect on the results obtained.

427 **4.1 Sample BC-47-4**

428 Sample BC-47-4 was drilled on site from section S47 (Fig. 1) between two blocks of the middle
429 ring of the bentonite barrier (Fig. 2), hence the core had a longitudinal interface. Although the
430 interface was not initially visible, upon trimming of the sample the two parts of it detached,
431 likely as a result of the pressure relief (Fig. SM4). The initial dry density and water content of
432 the specimen once trimmed were 1.59 g/cm³ and 24.8%, respectively.

433 This was one of the first samples tested and was only tested in the high-pressure, unsteady-
434 state (HP-US) equipment, following an unusual pressure path that consisted of these phases
435 (represented also in Fig. SM5):

- 436 – Phase 1: the injection pressure was set to values between 0.1 and 0.3 MPa and the
437 confining pressure was increased from 2 to 7 MPa; afterwards, keeping constant this
438 confining pressure, the injection pressure was increased up to 2.5 MPa.
- 439 – Phase 2: the confining pressure was increased from 7 to 9 MPa.
- 440 – Phase 3: the confining pressure was decreased from 9 to 3 MPa and then the injection
441 pressure was decreased to 1.5 MPa.

442 The permeability was computed from the evolution of pressure in the upstream and
443 downstream pressure cylinders. The duration of most of the steps was between 1 and 3 days,
444 although there were some steps that took very long, and thus the total duration of the test
445 was of 172 days. The permeability values computed from the pressure increase in the
446 downstream pressure cylinder are shown in Fig. 5 as a function of the injection pressure for
447 different confining pressures. In this case the effect of injection pressure on permeability was

448 not clear: for a constant confining pressure and for injection pressures lower than 0.8 MPa,
449 permeability decreased as injection pressure increased, but above this value, the permeability
450 remained constant or slightly increased. The duration of the steps could also have an influence
451 on the permeability measured, since it decreased noticeably when the confining pressure was
452 applied for a long time. Indeed the permeability decreased as the confining pressure
453 increased, although with a dispersion that can be explained by the effect of injection pressure
454 (which was not the same in all the steps), different duration of the steps and hysteresis on
455 loading-unloading cycles. However, when the confining pressure decreased down to 3 MPa
456 after loading up to 9 MPa, the permeability values measured were lower than the values
457 measured initially for similar or even higher confining pressures. This would mean that some
458 irreversible closure of gas pathways took place during consolidation. In fact, the interface
459 between the two halves of the specimen appeared completely sealed at the end of the test
460 (Fig. 6), and split only after drying in the oven.

461 **4.2 Sample BC-53-2**

462 This core sample from section S53 was drilled on site between two blocks in the inner ring of
463 the barrier, hence it had a longitudinal interface along the core. Although the interface was not
464 initially visible, after drying at the end of the test to determine the final water content of the
465 sample, the two parts of the core split open. The initial dry density of the sample was 1.63
466 g/cm³ and the water content 22.5%, corresponding to a degree of saturation of 93%.

467 The sample was first tested in the low-pressure equipment (LP), under confining pressures of
468 0.6 and 1.0 MPa. The pressure decrease in the upwards cylinder and the permeability values
469 computed from it are shown in Fig. 8. For a confining pressure of 0.6 MPa the gas permeability
470 tended to increase towards the end of the test, which could indicate that certain drying took
471 place because of the gas flow.

472 Afterwards, the sample was tested in the high-pressure steady-state equipment starting with
473 the last confining pressure applied in the LP equipment, 1.0 MPa. The stress path followed in
474 this test consisted of these phases (plotted in Fig. SM6):

475 – Phase 1: the test started at a confining pressure of 1.0 MPa and 0.2 MPa of injection
476 pressure. The injection pressure was increased from 0.2 to 0.4 MPa, keeping constant
477 confining pressure.

478 – Phase 2: the confining pressure was increased from 1.0 to 5.0 MPa, keeping an injection
479 pressure of 0.4 MPa.

480 – Phase 3: unloading of the sample to a pressure as low as the initial value.

481 During the increase of injection pressure from 0.2 to 0.4 MPa in Phase 1, the gas permeability
482 remained constant. However, the increase of confining pressure in Phase 2 caused a clear
483 decrease of gas permeability. Fig. 9 shows the effect of confining pressure on gas permeability
484 in both setups. The increase of confining pressure from 1 to 5 MPa caused a progressive
485 decrease of flow until no measurable flow took place for a confining pressure of 5 MPa. Then,
486 the sample was unloaded. During this phase, there was no measurable flow until the confining
487 pressure decreased to 2 MPa, when the gas permeability computed was an order of
488 magnitude lower than that for the same confining pressure during loading. This would indicate
489 that the consolidation effect was irreversible. In fact, the dry density increased during the test
490 from 1.63 to 1.64 g/cm³.

491 **4.3 Effect of injection and confining pressures**

492 The effect of injection pressure on permeability in the range of pressures tested was for most
493 samples negligible, as the two examples detailed above illustrated. In fact, the values
494 measured under different injection pressures for a given confining pressure were similar
495 among them and to the apparent gas permeability of each sample computed applying the
496 Klinkenberg correction (Villar et al. 2018a). This would mean that the Klinkenberg effect was

497 not relevant in the range of pressures applied, since they probably were high enough and
498 there was no slippage contribution to gas flow. In contrast, in the case of some samples with
499 the highest water content and lowest suctions, the increase in injection pressure caused a
500 clear increase in gas permeability. It was checked that for these samples flow was not linearly
501 related to the difference of squared pressures along the sample (P_{up} and P_{dw} in Eq. 8), which
502 indicates that Darcy's law should not strictly be applied to compute permeability (Villar et al.
503 2018a, Carbonell et al. 2019). Examples of linear and non-linear relations between flow and
504 $P_{up}^2 - P_{dw}^2$ are shown in Fig. SM7.

505 Taking this into account, the average values of gas permeability measured for consecutive
506 steps of different injection pressure under the same confining pressure have been plotted in
507 Fig. 10 to Fig. 12, for samples of the three sampling sections shown in Fig. 1. After reaching the
508 maximum confining pressure, corresponding to a value above which no measurable flow took
509 place, the samples were progressively unloaded. Exceptionally, in sample BC-53-1 the
510 maximum confining pressure (2.2 MPa) was determined by a technical failure and not by flow
511 cessation.

512 The distance to the gallery axis is indicated in the legend of the figures. Distances about 100
513 cm indicate that the sample was taken from the external ring of the barrier (the radius of the
514 gallery was 114 cm), values around 80 cm correspond to samples taken from the middle ring
515 and values around 60 cm correspond to samples taken from the inner ring, the one closest to
516 the heater.

517 For all the confining pressures applied the effective gas permeability decreased from the inner
518 part of the barrier towards the granite in all sections. Indeed, the samples taken from the
519 external ring of the barrier had the highest water contents and lowest dry densities. Overall,
520 the samples closest to the heater, which were drier and had lower degrees of saturation
521 (<90%), showed higher gas permeability. Section S53, which was close to the back end of the

522 heater (Fig. 1), had overall higher water content than the sections in the middle part of the
523 heater, where the temperatures were higher (Villar et al. 2020a). As a result, the samples from
524 the inner ring of section S53 had higher degrees of saturation than in the other sections (S_r
525 $>90\%$), and the permeability of these samples was in the order of the permeability of the
526 samples taken from the middle and external rings of the other sections (Fig. 12).

527 The samples with interface tended to have higher permeability than sound samples taken at
528 the same distance from the axis, particularly in the case of the inner ring. For example, the
529 comparison between samples BC-47-3 (no interface, $S_r=97\%$) and BC-47-4 (interface, $S_r=95\%$)
530 in Fig. 11 shows that the permeability of the sound sample was several orders of magnitude
531 lower than that of its interface-sample counterpart, tested under a higher confining pressure.
532 Although they were not tested under the same confining pressure, it is reasonable to assume
533 that the permeability of sample BC-47-4 would be even higher for a lower confining pressure
534 and consequently that under similar conditions the permeability of the sample with interface
535 would be higher than that of the sample without interface. In the samples from the external
536 and middle rings of the barrier the difference between samples with or without interface was
537 not so evident, except for the sample BC-53-4, which showed higher permeability than
538 expected. This was a highly saturated sample taken from the external ring of section S53,
539 whose interface was clearly visible during the preparation of the sample and quite open before
540 testing (Fig. 3). As a result, there would be more mechanical interference between the two
541 confronting sides, since the rugosity of the two halves would not exactly coincide after they
542 were separated and then put together again for the test. Sample BC-47-4 (see section 4.1),
543 which had an initially open interface, also recorded a very high permeability that drastically
544 decreased with the increase in confining pressure (Fig. 11).

545 The decrease of gas permeability with confining pressure was significant. For confining
546 pressures below 4 MPa most samples experienced a significant decrease in permeability as the

547 confining pressure went on increasing. For higher confining pressures the decrease was less
548 substantial, except when the sample had an interface. No flow took place through the samples
549 from the external and middle rings, those more saturated, for confining pressures higher than
550 3-4 MPa. In contrast, for the sample of the internal ring from section S44 (BC-44-7), the
551 confining pressure had to be increased up to 9.5 MPa to stop flow.

552 The permeability of samples with interface decreased steeply as the confining pressure
553 increased. The permeability of sample BC-47-4, decreased four orders of magnitude when the
554 confining pressure increased from 4 to 7 MPa, and sample BC-53-4, which had a similar degree
555 of saturation in section S53, showed an analogous behaviour. The behaviour of sample BC-44-
556 2, drilled between two blocks of the internal ring of section S44, was different, since its
557 permeability barely changed as the confining pressure was increased to 6 MPa, but decreased
558 three orders of magnitude when this value was exceeded, which probably indicates the closure
559 of the interface.

560 Overall, the samples that had higher initial permeability –either because their degree of
561 saturation was low or because they had an interface– had to be submitted to higher confining
562 pressures to stop flow. During unloading, as the confining pressure decreased the effective
563 permeability increased, but the original values were never recovered. The irreversibility of this
564 change was more noticeable in the samples with interface.

565 **4.4 Comparison with the reference bentonite**

566 The gas permeability of the reference FEBEX bentonite samples, compacted to different dry
567 densities with various water contents, was measured in previous researches and the
568 correlation between accessible void ratio and gas effective permeability shown in Equation 3
569 was obtained for samples with degrees of saturation lower than 97%. Those results and the
570 ones obtained in the FEBEX-DP samples summarised in the previous section have been plotted
571 in Fig. 13. These values were obtained in the same setups as the values obtained for the

572 reference sample. In order to make the results strictly comparable, only those values obtained
573 under confining pressures of 0.6 and 1.0 MPa have been represented. Nevertheless, it was
574 observed that, for any of the confining pressures applied, the permeability tended to be higher
575 the higher the accessible void ratio (Villar et al. 2018a). The accessible void ratio of the FEBEX-
576 DP samples were overall very low (below 0.15), in the low range of the FEBEX samples,
577 because their degree of saturation was very high. Nevertheless, the new values obtained in
578 samples submitted for 18 years to barrier conditions are consistent with those of the reference
579 bentonite, or maybe in the lower range. The scatter in the data was high because the range of
580 dry densities and water contents involved was large and there were also samples with and
581 without interface.

582 For the higher values of accessible void ratio, the samples with interface had higher
583 permeabilities than those computed with Eq. 3, whereas for the lower accessible void ratios
584 there was not a clear difference between samples with or without interface, and both were
585 closer to those of the reference bentonite. This was observed for all the range of confining
586 pressures tested. An exception was sample BC-53-4, which was drilled in the external ring of
587 the barrier and consequently had a low accessible void ratio, but showed higher permeability
588 than expected, probably because of the exceptionally open interface at the beginning of the
589 test, as discussed above.

590 **4.5 Final state: microstructural changes**

591 Final checking of water content along the samples showed that the gravimetric water content
592 was usually lower in the upper part, from where gas was injected (although the differences
593 inside a given sample were lower than 0.5%). This indicates that certain drying of the upper
594 part of the samples took place as a consequence of gas injection, the water being pushed by
595 the gas towards the bottom of the samples. In some cases, particularly in the samples with
596 higher initial water content, water could have been expelled out of the sample, because the
597 final water content was found to be lower than the initial one (on average $3.2\pm 3.8\%$), both in

598 samples with and without interface. However, no liquid water outflow was actually observed
599 in any test. In fact, it cannot be ruled out that at least part of the decrease in water content at
600 the end of the test observed in some samples could have taken place during the initial
601 trimming process of the cores (see section 3.2).

602 At the end of the tests the dimension of the samples were measured and it was checked that,
603 in most cases, the dry density of the samples had increased, which is consistent with the
604 decrease in effective gas permeability occurred during the tests (section 4.3). The dry density
605 of the samples increased after testing in all those tests in which the maximum confining
606 pressure applied was higher than 2.5 MPa (except samples BC-47-1, BC-44-4 and BC-53-3). In
607 fact, there is a positive linear correlation between the change in dry density and the maximum
608 pressure applied ($R^2=0.6$), but the increase was more notable for maximum confining
609 pressures below 5 MPa (Fig. 14).

610 The pore size distribution of some of the samples was determined by mercury intrusion
611 porosimetry before and after gas testing. A spare fragment resulting from the sample
612 preparation and a fragment from the sample at the end of the test were used. The aim of
613 these tests was to analyse the effect of gas flow on the pore size distribution of the bentonite.

614 The mercury intrusion method allows access to be gained only to part of the macroporosity
615 (pores between 600 μm and 50 nm) and to part of the mesopores (those of sizes between 50
616 and 6 nm), since mercury does not intrude the microporosity (pores of a size of less than 2 nm,
617 according to the classification of Sing et al. 1985). In the high-density clay materials retrieved
618 from the FEBEX-DP, pores larger than those that can be quantified by MIP are not expected.
619 Considering that most of the non-intruded porosity corresponds to the pores of a size smaller
620 than the limit of the apparatus, an estimation of the percentage of pores actually intruded can
621 be made by comparing the actual void ratio of the samples (e , computed from their dry density

622 and density of solid particles) and the apparent void ratio calculated from mercury intrusion
623 (e_{nw} , mercury being a non-wetting [nw] fluid).

624 The curves corresponding to a sample before and after gas testing are shown Fig. 15. The
625 figure on the left shows the cumulative intruded void ratio. These void ratios have been
626 corrected to take into account the percentage of pores not intruded by mercury. The total void
627 ratio of the samples is indicated in the figure by dotted horizontal lines. The void ratio actually
628 intruded was in all samples of only about 50%, which would mean that the percentage of pores
629 smaller than 6 nm or not interconnected was very relevant. All the samples experienced
630 certain decrease in void ratio (increase in dry density) after gas testing, which is attributed to
631 the compression exerted by the confining pressure applied (Fig. 14). The figure on the right
632 shows the incremental mercury intrusion over the range of pore sizes explored in the tests.
633 Two pore families appeared systematically in all the samples, one in the size range of
634 macropores and another one in the size range of mesopores. Overall the curves before and
635 after gas testing were similar for each sample, and only the samples from the external ring,
636 with very high degrees of saturation (e.g. BC53-4 in Fig. 15), showed a clear increase in the size
637 mode of the macropores after gas testing (Villar et al. 2018a).

638 From these curves, the void ratio corresponding to pores of diameter higher or smaller than 50
639 nm (i.e. macropores and meso+micropores), can be obtained. The results have been plotted in
640 Fig. 16 as a function of the distance to the gallery axis of the sample. There was an overall
641 decrease in the macropore void ratio after gas testing, whereas the void ratio corresponding to
642 pores <50 nm did not clearly change. In terms of the proportion of total void ratio
643 corresponding to each of these pore sizes, the percentage of macropores decreased after gas
644 testing while the percentage of pores <50 nm increased. Hence, the increase in dry density
645 observed in most samples after gas testing (Fig. 14) would have been achieved by the decrease
646 in macropore volume. The interfaces did not seem to affect these pore size distribution

647 changes. Concerning the size of the pores, in the samples from the external ring the size of the
648 macropores increased after gas testing, which could be connected with the opening of
649 pathways, because the accessible void ratio in these samples was very low. In contrast, the size
650 of the mesopores did not change in a clear consistent way during gas testing.

651 The percentage of void ratio change occurred during gas testing for pores larger and smaller
652 than 50 nm is shown in Fig. 17 as a function of the maximum confining pressure reached
653 during gas testing. The higher the confining pressure applied the higher the decrease in
654 macropore void ratio, whereas smaller pores did not seem to change coherently with confining
655 pressure. These results agree well with the change of dry density as a consequence of the
656 confining pressure applied during gas testing, which was significant for confining pressures
657 higher than 2 MPa. Since the samples for which the pore size distribution was analysed had
658 been subjected to confining pressures higher than this value, the total void ratio, and
659 particularly the void ratio corresponding to macropores, decreased in all of them.

660 **5 Discussion**

661 In the previous sections results of the gas permeability measurements performed in samples
662 retrieved from the FEBEX in situ tests have been presented. The water content and dry density
663 of the bentonite changed across the barrier as a function of the distances to the heater and
664 the granite. Consequently, the samples taken closest to the heater had lower water content
665 and higher dry density, whereas the samples taken closest to the granite had the highest water
666 content and lowest dry density. The effective gas permeability of the samples decreased with
667 the increase of water content and the decrease in dry density and tended to be lower towards
668 the granite, where the degree of saturation was higher.

669 During the tests, the gas flow observed was steady in most cases and no effect of the injection
670 pressure on the permeability values was detected, except for a few of the more saturated

671 samples, for which gas permeability increased with increasing gas injection pressure (in fact
672 this behaviour was clear only in sample BC-53-3), indicating non-Darcian flow. Additionally, it
673 was checked that the Klinkenberg effect was not significant in the range of pressures applied
674 (Villar et al. 2018a).

675 However, the gas permeability was clearly affected by the stress state. It decreased noticeably
676 with the increase in confining pressure up to 4 MPa, particularly for the wetter samples, those
677 taken closer to the granite. Beyond a confining stress of 9 MPa no gas flow took place through
678 any of the wetter samples, hence the breakthrough pressure for them would be higher than
679 this value, which in turn is higher than the expected swelling pressure (Eq. 2). In fact, gas
680 breakthrough pressures higher than the swelling pressure were measured in the FEBEX
681 reference bentonite compacted and tested under isochoric conditions (Gutiérrez-Rodrigo et al.
682 2021). In contrast, flow took place through the drier samples, even for confining pressures as
683 high as 9 MPa. The consolidation induced by the increase in confining pressure increased the
684 degree of saturation of the samples and reduced their suction, taking them back to a stress
685 state closer to that in the barrier during the in situ test. At the end of operation of the FEBEX in
686 situ test total pressures above 2 MPa were measured in the intermediate bentonite ring and
687 higher than 5 MPa in the outer part of the barrier (Martínez et al. 2016, Villar et al. 2020b),
688 and this could indicate that during operation the stress state in the barrier was high enough as
689 to limit gas migration.

690 The confining stress reduced the size of the gas pathways, also increasing their tortuosity. In
691 the case of the less saturated samples there was insufficient moisture to reduce or block the
692 air-filled pore network of the specimens and minimise gas flow, and the gas found ways out
693 until the confining pressure was enough to sufficiently reduce the air-filled pore space. In
694 contrast, in the highly-saturated samples there was no need of applying a high confining
695 pressure to completely block the air passages, which already were small and tortuous. This

696 also would explain the fact that the effect of injection pressure increase was only noticeable in
697 the samples with the highest water content, in which small changes in the size of the cross-
698 section of the gas pathways would trigger significant changes in very low permeability.

699 The decrease in permeability occurred during loading was not reversible, and the gas
700 permeability of the samples after unloading was lower than the initial one. Most of the
701 samples experienced during operation in the barrier an increase in void ratio as a result of
702 hydration and swelling, which led to the reduction of the initial dry density of the blocks (1.7
703 g/cm³) to the average dry density of the barrier (1.6 g/cm³). Consequently the apparent
704 preconsolidation stress of the bentonite decreased during in situ operation, whereas the pre-
705 yield and post-yield compressibility values increased (Romero et al. 2017, included in Villar
706 2017). This would explain the fact that the samples consolidated easily during gas testing. In
707 fact, the dry density of the samples at the end of the tests in which confining pressures higher
708 than 2 MPa were applied was higher than the initial one.

709 The pore size distribution analyses carried out by mercury intrusion porosimetry showed a
710 decrease in the macropore void ratio in all the samples tested applying confining pressures
711 higher than 2 MPa. This decrease was more significant as the confining pressure applied during
712 gas testing was higher, which would mean that the compression exerted by the confining
713 pressure was mostly absorbed by the macropores. In some of the wetter samples an increase
714 of the size of the macropores was observed after gas testing, which could correspond to the
715 opening of pathways allowing gas flow, given the very low accessible void ratio of these nearly
716 saturated samples. González-Blanco et al. (2016a, 2016b) observed a new family of pores at
717 entrance sizes larger than 2 µm after gas injection in samples of argillaceous rock formations.
718 These pores were associated with fissure opening and would act as preferential air pathways.
719 They were observed by microcomputed tomography, both in a clay rock (González-Blanco et
720 al. 2017a) and in bentonite (González-Blanco et al. 2017b). Harrington et al. (2017) analysed

721 the stress field measured during a gas injection test in saturated compacted bentonite and
722 inferred from it that the gas pathways were created by dilatancy and propagated through the
723 clay in response to variations in applied gas pressure.

724 The gas permeability of the FEBEX reference bentonite is mainly related to the void ratio
725 accessible for gas flow, $e(1-S_r)$, which depends on water content and dry density (see section
726 Background: gas transport studies in FEBEX bentonite). For the FEBEX-DP samples, because of
727 the high water saturation of most of the barrier after the long operation period, the accessible
728 void ratio was below 0.15, and decreased towards the external part of the barrier, where the
729 degree of saturation was higher. For these samples the decrease of gas permeability with
730 accessible void ratio roughly followed the empirical relation of Eq. 3, which predicts an acute
731 decrease of gas permeability in the low range of accessible void ratios. In fact, the drop in
732 effective gas permeability when approaching full saturation is that of several orders of
733 magnitude (Fig. 13). Therefore, it seems that no changes on the gas transport properties of the
734 bentonite matrix took place during operation.

735 However, samples with an interface drilled in the internal ring of the barrier had higher
736 permeability than samples of similar accessible void ratio with no interface, and it was
737 necessary to apply higher confining pressures to reduce or suppress gas flow in them. In fact
738 the presence of an interface had higher relevance than the accessible void ratio on the gas
739 permeability, probably because the gas transport mechanisms in both kinds of samples were
740 not the same: flow took place through the accessible porous structure, but in the samples with
741 interface it preferentially occurred along the interface, likely following “models” of flow in
742 deformable rock fractures, in which liquid flow takes place according to a local cubic law or its
743 variations. The sudden decreases in permeability occurred in some samples when confining
744 pressure was increased beyond a given value would correspond to the closing of the interface
745 as a preferential pathway. In contrast, wetter samples drilled along interfaces of the

746 intermediate and external rings of the barrier (which had very low accessible void ratio, lower
747 than 0.08, because of the high saturation), had permeabilities closer to those corresponding to
748 the same accessible void ratio in the reference bentonite. In fact, in these samples the
749 interfaces were barely visible and looked like sealed before gas testing.

750 Popp et al. (2014) tested the interface between blocks manufactured from a bentonite/sand
751 (60/40) mixture. Under dry conditions, gas flow along the interfaces was at least four orders of
752 magnitude higher than through the matrix. An increase in confinement significantly lowered
753 the gas flow but the effect was more pronounced for interfaces than for the matrix. They
754 saturated the blocks assemblages and performed gas injection and shear tests to check the
755 behaviour of the interface. The authors concluded that the interface perfectly healed after
756 saturation, which was physically verified by the development of cohesion after saturation. All
757 these observations are consistent with the findings reported in this work. Gas breakthrough
758 tests performed in saturated samples of FEBEX bentonite under isochoric conditions showed
759 that samples with an interface behaved as samples of the same dry density with no interface,
760 finding in both cases breakthrough pressure values related to dry density. The conclusion was
761 that after material homogenization the interface was not a preferential pathway, neither for
762 water nor for gas (Gutiérrez-Rodrigo 2018, Gutiérrez-Rodrigo et al. 2021).

763 Previous laboratory studies showed that, in the FEBEX compacted bentonite, two-phase flow
764 through stable pathways seemed to take place for degrees of saturation lower than about
765 97%, since in these samples gas flow was stable for a given pressure gradient. For higher
766 degrees of saturation pathway dilation could be the predominant mechanism (Villar et al.
767 2013, Gutiérrez-Rodrigo 2018). Graham et al. (2002) found that this threshold was 93% for a
768 sodium bentonite, and that below this degree of saturation there was only small resistance to
769 gas migration. Tests performed in compacted saturated samples under isochoric conditions
770 showed that the threshold pressure for gas entry into the bentonite was higher than the

771 swelling pressure and seemed to be lower than the gas pressure required for fracturing
772 (macroscopically) the material (Gutiérrez-Rodrigo et al. 2021). In contrast, in the research
773 reported here, two-phase flow seems to have taken place in most cases, even for samples with
774 degree of saturation higher than 97%. The fact that these samples were tested under constant
775 confining stress (in triaxial cells) instead of under no volume change conditions (isochoric),
776 would have made easier the transport of gas, with opening of trajectories for gas flow that
777 could not be opened under isochoric conditions. Hence, the testing conditions seem to have an
778 influence on the results obtained. Graham et al. (2016) concluded from gas injection tests in
779 saturated compacted bentonite that the degree of compressibility of the clay and the stress
780 conditions may be an important control on the approach to gas breakthrough in the buffer. In
781 this line, Xu et al. (2015) performed laboratory tests in a saturated, low permeability clay that
782 showed that the failure of the sealing efficiency was closely related to the difference between
783 the gas injection pressure and the confining pressure.

784 **6 Concluding remarks**

785 The FEBEX in situ test reproduced the engineered barrier system of an underground repository
786 for nuclear waste and was running under natural hydration from the granitic host rock and
787 heating from the simulated canister, for 18 years. The barrier was composed of bentonite
788 blocks and had an average dry density of 1.6 g/cm^3 . In 2015 the heater was switched off, the
789 experiment was dismantled and bentonite samples were taken at different positions around
790 the heater. Some of these samples were drilled between two blocks, therefore they had an
791 interface along the core. The gas permeability of the samples was measured in custom-built
792 setups using nitrogen as gas, without artificially saturating the samples prior to or during gas
793 testing, and checking the effect of injection and confining pressures.

794 Except for some of the most saturated samples, stable gas flow took place for any of the
795 boundary conditions applied. The reduction of gas permeability with confining pressure

796 resulted from the decrease in the volume of macropores, and was particularly significant for
797 the more saturated samples, i.e. those from the external part of the barrier. Higher gas
798 permeability values were measured in the samples taken close to the heater, which were drier,
799 and particularly in those with interface. However, the gas permeability of the more saturated
800 samples was related to the gas accessible void ratio (related in turn to bentonite water content
801 and dry density), irrespective of the presence of interface, which attest the healing of the
802 contacts between blocks as a result of saturation.

803 The effective permeability values obtained are probably conservative, since they were
804 obtained for stress situations maintained for relatively short periods of time (a few hours),
805 whereas in some cases it was checked that gas permeability was lower if the samples were
806 compressed for longer periods of time. It is also possible that temperatures in the range of
807 those expected around the canisters of a real repository have an effect on gas permeability,
808 and this aspect has not been checked, since all the measurements were performed at
809 laboratory temperature.

810 The results obtained suggest that the gas generated in the proximity to the waste containers
811 would be able to move by advection as long as the bentonite around it remains unsaturated,
812 more easily along interfaces. However, it is likely that in a real repository even the drier
813 interfaces in the internal part of the bentonite barrier would not be preferential gas pathways
814 once the external part of the barrier is saturated, because the high stresses in the system
815 would close them. In any case, the external, fully saturated part of the barrier would block gas
816 movement away from the barrier, and gas would only be able to escape slowly by diffusion in
817 the pore water or suddenly by breakthrough if gas pressure builds up above a value that would
818 be higher than the swelling pressure but very dependent on the stress conditions. The role of
819 the interfaces on gas transport would only be relevant for low degrees of saturation, i.e. at the
820 beginning of operation or close to the heater. Nevertheless, since gas generation would be

821 triggered by processes implying high water contents, it is not expected to be relevant until
822 advance stages of the repository life, when the interfaces between blocks in all the barrier will
823 have been sealed as a result of full saturation.

824

825 **Acknowledgements**

826 The research leading to these results was financed through the Annex XLII of the ENRESA-
827 CIEMAT framework agreement and by the FEBEX-DP consortium (NAGRA, SKB, POSIVA,
828 CIEMAT, KAERI.) The preparation of this paper was performed in the framework of the EURAD
829 project – WP6 GAS (<http://www.ejp-eurad.eu/>), which receives funding from the European
830 Union’s Horizon 2020 research and innovation programme under grant agreement No 847593.
831 Part of the laboratory work was carried out by J. Aroz, R.J. Iglesias, and F.J. Romero. The
832 control and data acquisition systems for the gas permeability tests were developed by Dr. J.M.
833 Barcala of CIEMAT. The mercury intrusion porosimetry tests were performed at the
834 Petrophysical laboratory of CIEMAT by N. Brea, supervised by Dr. R. Campos. Beatriz Carbonell
835 was hired in the framework of the . , with financing of the European Social Fund and the Youth
836 Employment Initiative.

837

838 **References**

839 Bárcena, I., García-Siñeriz, J.L. 2015. FEBEX-DP (GTS) Full Dismantling Sampling Plan (in situ
840 Experiment). Nagra Arbeitsbericht NAB 15-14. 103 pp.

841 Carbonell, B., Villar, M.V., Martín, P.L., Gutiérrez-Álvarez, C. 2019. Gas transport in compacted
842 bentonite after 18 years under barrier conditions. Geomechanics for Energy and the
843 Environment 17: 66-74. <https://doi.org/10.1016/j.gete.2018.03.001>

844 ENRESA 2006. FEBEX Full-scale Engineered Barriers Experiment, Updated Final Report 1994-
845 2004. Publicación Técnica ENRESA 05-0/2006, Madrid, 590 pp.

846 García-Siñeriz J.L., Abós H., Martínez V., de la Rosa C., Mäder U., Kober F. 2016. FEBEX-DP:
847 Dismantling of the heater 2 at the FEBEX “in situ” test. Description of operations. Nagra
848 Arbeitsbereich NAB16-011. Wettingen, Switzerland, 92 pp.

849 Gonzalez-Blanco, L., Romero, E., Jommi, C., Li, X., Sillen, X., 2016a. Gas migration in a Cenozoic
850 clay: Experimental results and numerical modelling. *Geomechanics for Energy and the*
851 *Environment* 6: 81–100.

852 Gonzalez-Blanco, L., Romero, E., Li, X., Sillen, X., Jommi, C. 2016b. Air injection tests in two
853 argillaceous rock formations: experimental results and modelling. *Proceedings of the 1st*
854 *International Conference on Energy Geotechnics, ICEGT 2016, Kiel, Germany, 29-31 August*
855 *2016*. CRC Press, pp. 715-721. ISBN 9781138032996. DOI [10.1201/b21938-112](https://doi.org/10.1201/b21938-112)

856 Gonzalez-Blanco, L., Romero, E., Jommi, C., Sillen, X., Li, X. 2017a. Exploring Fissure Opening
857 and Their Connectivity in a Cenozoic Clay During Gas Injection. In: Ferrari, A. Laloui, L. (eds.):
858 *Advances in Laboratory Testing and Modelling of Soils and Shales (ATMSS)*, Springer Series in
859 *Geomechanics and Geoengineering*, pp. 288-295. Springer, Cham, Switzerland. ISBN 978-3-
860 319-52772-7. DOI [10.1007/978-3-319-52773-4_33](https://doi.org/10.1007/978-3-319-52773-4_33)

861 Gonzalez-Blanco, L.; Romero, E.; Marschall, P. 2017b. Pathway development and connectivity
862 during gas injection / dissipation tests: experimental results and numerical modelling.
863 *Interpore 2017: 9th International Conference on Porous Media & Annual Meeting*.

864 Graham, J., Halayko, K.G., K.G., Hume, H., Kirkham, T., Gray, M., Oscarson, D. 2002. A
865 capillarity-advective model for gas break-through in clays. *Engineering Geology* 64: 273-286.

866 Graham, C.C., Harrington, J.F., Sellin, P. 2016. Gas migration in pre-compacted bentonite under
867 elevated pore-water pressure conditions. *Applied Clay Science* 132-133: 353-365.
868 <http://dx.doi.org/10.1016/j.clay.2016.06.029>

869 Gutiérrez-Rodrigo, V. 2018. Transporte de gas en materiales de barrera. Tesis Doctoral.
870 Universidad Complutense de Madrid. Colección Documentos CIEMAT. ISBN: 978-84-7834-802-
871 2. Madrid, 303 pp.

872 Gutiérrez-Rodrigo, V., Villar, M.V., Martín, P.L., Romero, F.J., Barcala, J.M. 2015. Gas-
873 breakthrough pressure of FEBEX bentonite. In: Shaw, R. P. (ed.) Gas Generation and Migration
874 in Deep Geological Radioactive Waste Repositories. Geological Society, London, Special
875 Publications, 415, 47-57. First published online November 14, 2014.
876 <http://dx.doi.org/10.1144/SP415.4>.

877 Gutiérrez-Rodrigo, V., Martín, P.L., Villar, M.V. 2021. Effect of interfaces on gas breakthrough
878 pressure in compacted bentonite used as engineered barrier for radioactive waste disposal.
879 Process Safety and Environmental Protection 149: 244-257.
880 <https://doi.org/10.1016/j.psep.2020.10.053>.

881 Harrington, J.F. and Horseman, S.T., 2003. "Gas migration in KBS-3 buffer bentonite: sensitivity
882 of test parameters to experimental boundary conditions." Report TR-03-02. Svensk
883 Kärbränslehantering AB (SKB), Stockholm, Sweden.

884 Harrington, J.F., Graham, C.C., Cuss, R.J., Norris, S. 2017. Gas network development in a
885 precompacted bentonite experiment: Evidence of generation and evolution. Applied Clay
886 Science 147: 80-89.

887 Horseman, S.T., Harrington, J.F., Sellin, P. 1999. Gas migration in clay barriers. Engineering
888 Geology 54: 139-149.

889 Martínez, V., Abós, H., García-Siñeriz, J.L. 2016. FEBEX-e: Final Sensor Data Report (FEBEX In
890 Situ Experiment). Nagra Arbeitsbericht NAB 16-019. Madrid, 244 pp.

891 Olivella S., Alonso E.E. 2008. Gas flow through clay barriers. Géotechnique 58(3): 157–176.

892 Ortiz, L., Volckaert, G., Mallants, D. 2002. Gas generation and migration in Boom Clay, a
893 potential host rock formation for nuclear waste storage. *Engineering Geology* 64: 287-296.

894 Lloret, A. 1982. Comportamiento deformacional del suelo no saturado bajo condiciones
895 drenadas y no drenadas. Ph. D. Thesis. Universidad Politécnica de Cataluña.

896 Loosveldt, H., Lafhaj, Z., Skoczylas, F. 2002. Experimental study of gas and liquid permeability
897 of a mortar. *Cement and Concrete Research* 32: 1357–1363.

898 Popp, T., Rölke, C. y Salzer, K. (2014). Hydromechanical properties of bentonite-sand block
899 assemblies with interfaces in engineered barrier systems. En R.P. Shaw (Ed.), *Gas Generation*
900 *and Migration in Deep Geological Radioactive Waste Repositories*. Geological Society, London,
901 *Special Publications*, 415: 19-33.

902 Romero, E., Alvarado, C. Lloret, A., Mirsalehi, S. 2017. Laboratory tests on the post mortem
903 hydro-mechanical characterisation of FEBEX bentonite. CIMNE-UPC-GEOLAB, 84 pp.

904 Scheidegger, A.E. 1974. *The Physics of Flow Through Porous Media*, 3rd ed. University of
905 Toronto Press, Toronto.

906 Sellin, P., Leupin, O., 2013. The use of clays as an engineered barrier in radioactive-waste
907 management – a review. *Clay Clay Miner.* 61 (6): 477–498.
908 <https://doi.org/10.1346/CCMN.2013.0610601>

909 Sing, K.S.W., Everett, D.H., Haul, R.A.W., Moscou, L., Pierotti, R.A., Rouquérol, J.,
910 Siemieniewska, T. 1985. Reporting physisorption data for gas/solid systems with special
911 reference to the determination of surface area and porosity. *Pure Appl. Chem.* 57(4): 603-619.
912 IUPAC.

913 Villar, M.V. 2002. Thermo-hydro-mechanical characterisation of a bentonite from Cabo de
914 Gata. A study applied to the use of bentonite as sealing material in high level radioactive waste
915 repositories. *Publicación Técnica ENRESA 01/2002*, Madrid, 258 pp.

916 Villar, M.V.(Ed). 2017. FEBEX-DP Postmortem THM/THC Analysis Report. NAB 16-017. 143 pp.

917 Villar, M.V., Lloret, A. 2001. Variation of the intrinsic permeability of expansive clay upon
918 saturation. In: Adachi, K., Fukue, M. (eds.): Clay Science for Engineering. Balkema, Rotterdam.
919 259-266.

920 Villar, M.V., García-Siñeriz, J.L., Bárcena, I., Lloret, A., 2005. State of the bentonite barrier after
921 five years operation of an in situ test simulating a high level radioactive waste repository. Eng.
922 Geol. 80 (3–4): 175–198. <https://doi.org/10.1016/j.enggeo.2005.05.001>.

923 Villar, M.V., Gutiérrez-Rodrigo, V., Martín, P.L., Romero, F.J., Barcala, J.M. 2013. Gas transport
924 in bentonite. Informes Técnicos CIEMAT 1301. Madrid, 63 pp. DOI:
925 10.13140/RG.2.2.14334.28489

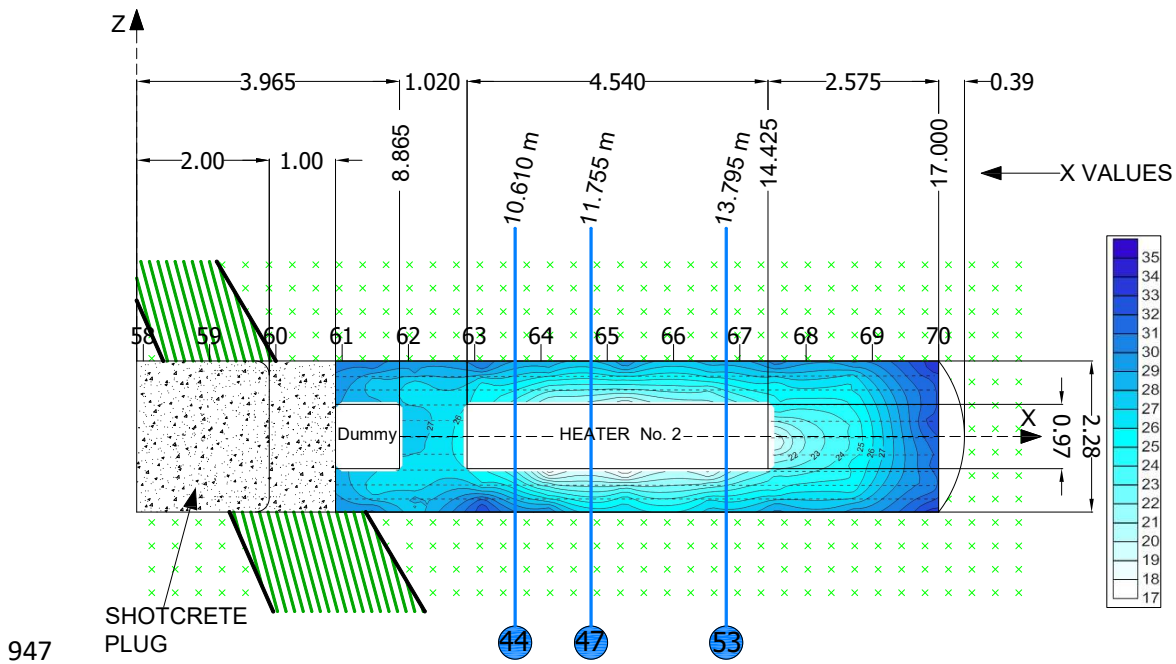
926 Villar, M.V., Iglesias, R.J., Abós, H., Martínez, V., de la Rosa, C., Manchón, M.A. 2016. FEBEX-DP
927 onsite analyses report. NAB 16-012. 106 pp.

928 Villar, M.V., Carbonell, B., Martín, P.L., Gutiérrez-Álvarez, C., Barcala, J.M. 2018a. Gas
929 permeability of bentonite samples of the FEBEX Dismantling Project (FEBEX-DP). Informes
930 Técnicos CIEMAT 1431. Madrid, 89 pp.

931 Villar, M.V., Iglesias, R.J., Gutiérrez-Álvarez, C., Carbonell, B., Campos, R., Campos, G., Martín,
932 P.L., Castro, B. 2018b. FEBEX-DP: Thermo-hydro-mechanical postmortem analysis of bentonite
933 performed at CIEMAT. Technical report CIEMAT/DMA/2G216/2/16. NAB16-024. Madrid, 134
934 pp.

935 Villar, M.V., Iglesias, R.J., García-Siñeriz, J.L. 2020a. State of the in situ Febex test (GTS,
936 Switzerland) after 18 years: A heterogeneous bentonite barrier after 18 years operation.
937 Environmental Geotechnics 7(2): 147-159. <https://doi.org/10.1680/jenge.17.00093>

- 938 Villar, M.V., Iglesias, R.J., García-Siñeriz, J.L., Lloret, A., Huertas, F. 2020b. Physical evolution of
939 a bentonite buffer during 18 years of heating and hydration. *Engineering Geology* 264: 105408.
940 <https://doi.org/10.1016/j.enggeo.2019.105408>
- 941 Xu, L., Ye, W.M., Ye, B., Chen, B., Chen, Y.G., Cui, Y.J. 2015. Investigation on gas migration in
942 saturated materials with low permeability. *Engineering Geology* 197: 94-102.
- 943 Yoshimi, Y., Osterberg, J.O. 1963. Compression of partially saturated cohesive soils. *J. Soil*
944 *Mechanics and Foundations Division*. ASCE 89, SM 4, 1-2.
- 945
- 946



948 **Fig. 1:** Layout of the FEBEX in situ test during the second operational phase and location of the
 949 sampling sections from which the samples for the gas transport tests were taken (distances in m,
 950 modified from B rcena and Garc a-Si neriz 2015). The contour lines correspond to the water content of
 951 the bentonite determined upon dismantling (Villar et al. 2016)

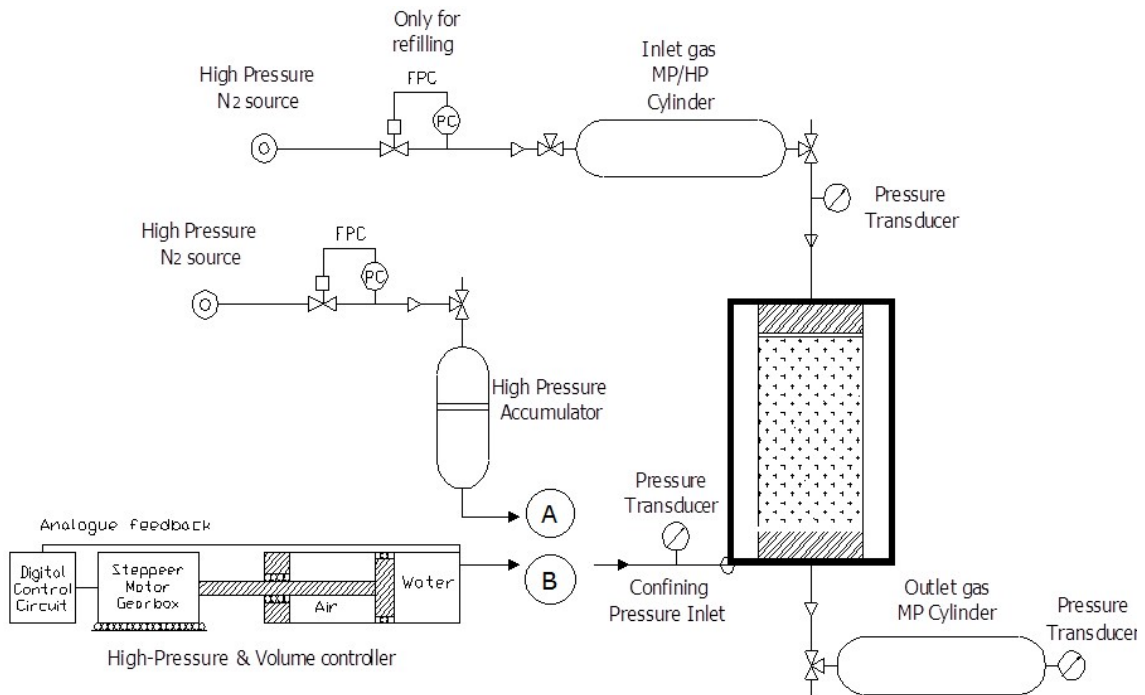


953 **Fig. 2:** Appearance of the bentonite barrier around Heater #2 during installation in 1997 and during
 954 dismantling in 2015 (the block contours were difficult to tell apart and have been indicated by
 955 discontinuous lines.) Examples of the location of samples drilled for gas testing are marked with
 956 circles



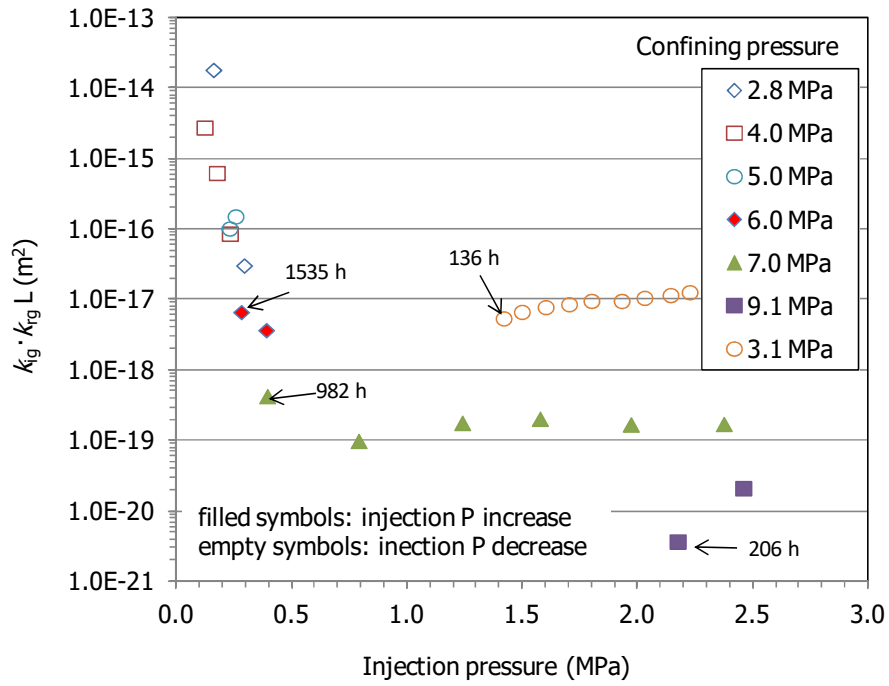
957

958 **Fig. 3: Initial appearance of sample BC-53-4**



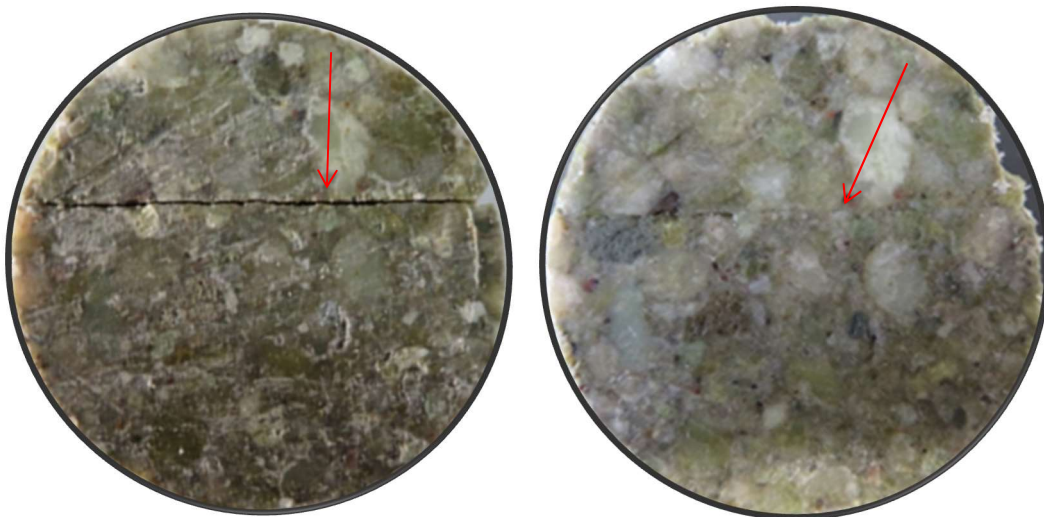
959

960 **Fig. 4: Schematic diagram of the setup for the high-pressure unsteady equipment (HP-US) with the**
 961 **two options for applying confining pressure: A) HP accumulator; B) P/V controller**



962

963 Fig. 5: Gas permeability at constant confining pressure for sample BC-47-4 (the duration of longer
964 steps is indicated in hours.) Confining pressure was changed in the order indicated in the legend



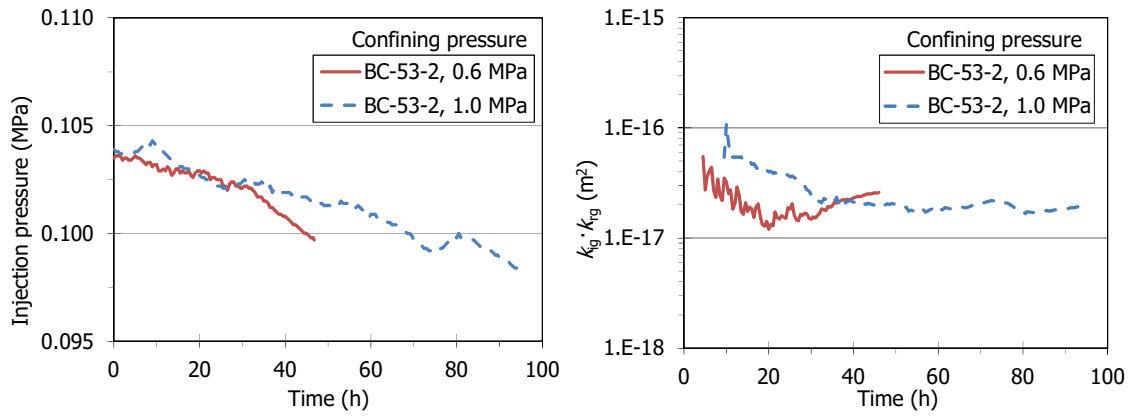
965

966 Fig. 6: Initial and final appearance of sample BC-47-4 (the arrows indicate the same position before
967 and after testing)



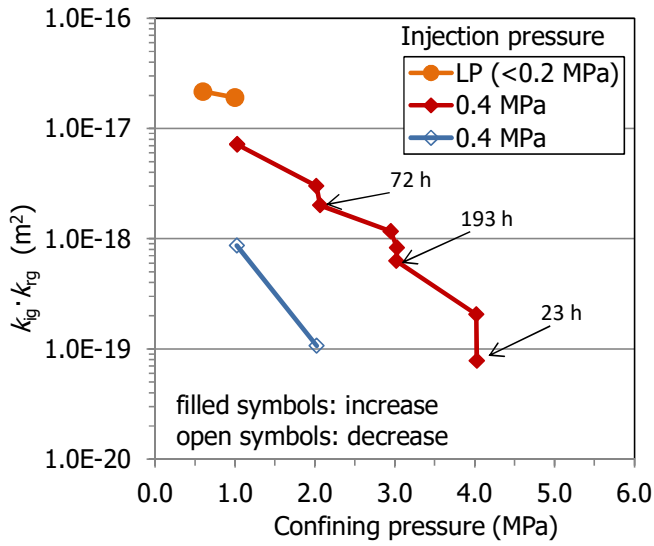
968

969 **Fig. 7: Appearance of sample BC-53-2 before (left) and after (middle) gas testing. The interface split**
 970 **only after drying in the oven (right)**



971

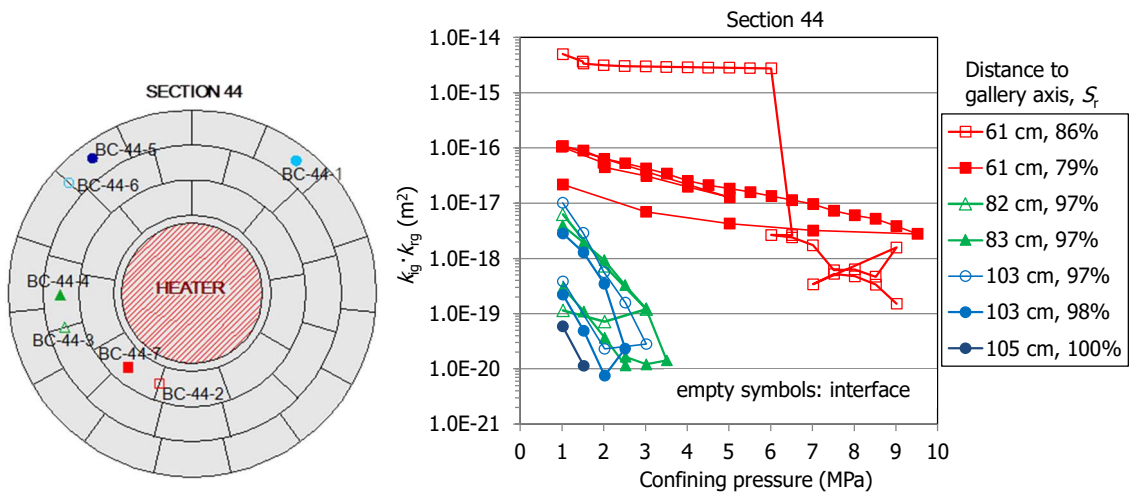
972 **Fig. 8: Evolution of injection pressure and gas effective permeability ($k_{ig} \cdot k_{rg}$) in the low pressure**
 973 **equipment (LP) for sample BC-53-2 (injection gas pressure given in relative values)**



974

975 **Fig. 9: Evolution of gas effective permeability at constant injection pressure (Phase 2 and 3) for sample**

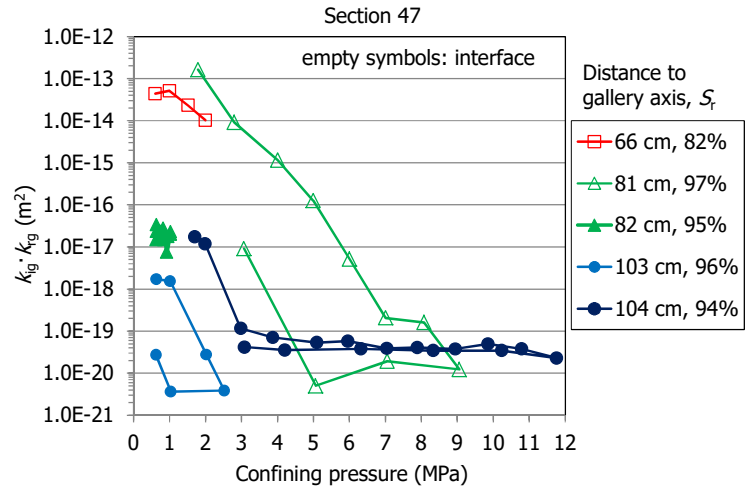
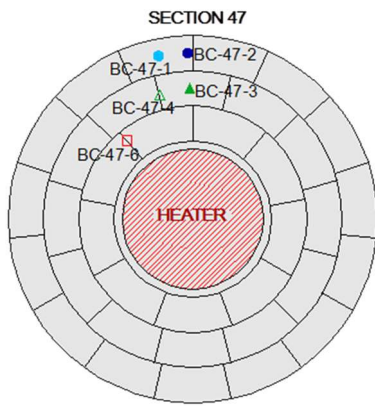
976 **BC-53-2. The duration of the longer steps is indicated**



977

978 **Fig. 10: Change of effective gas permeability with increase/decrease of confining pressure for samples**

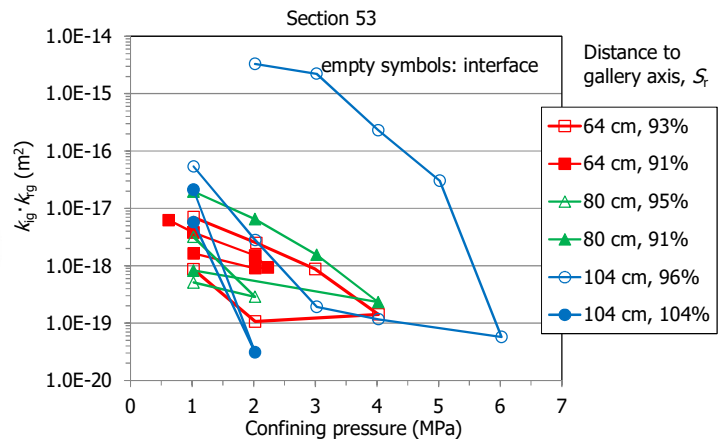
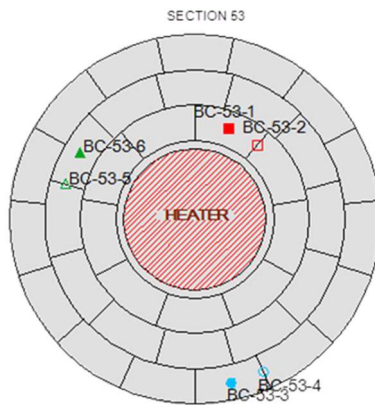
979 **from section S44 (flow was not steady in sample BC-44-5)**



980

981 Fig. 11: Change of effective gas permeability with increase/decrease of confining pressure for samples

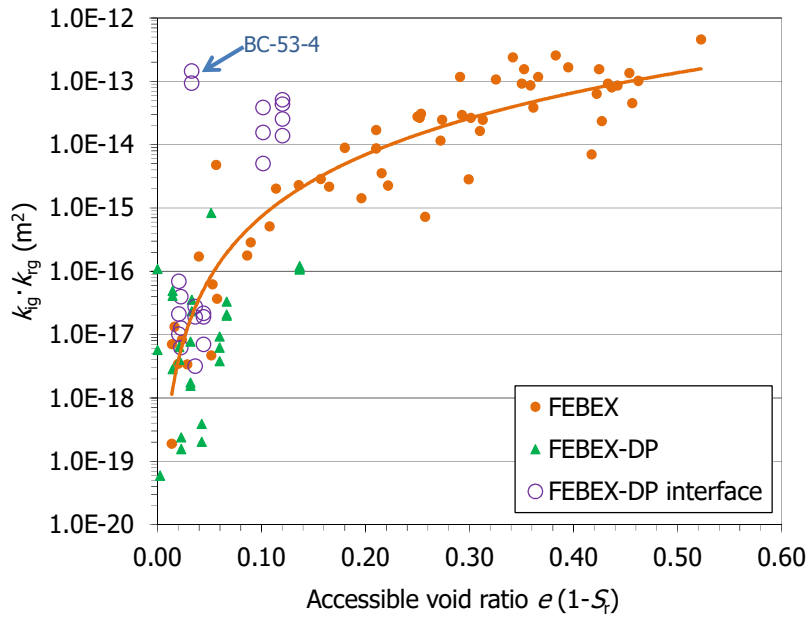
982 from section S47



983

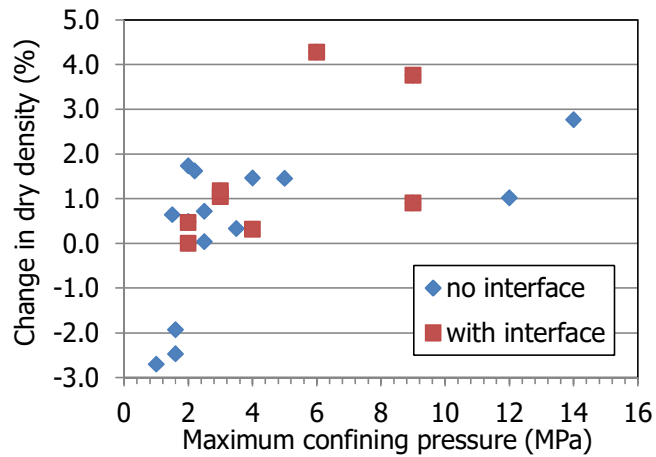
984 Fig. 12: Change of effective gas permeability with increase/decrease of confining pressure for samples

985 from section S53 (flow was not steady in sample BC53-3)



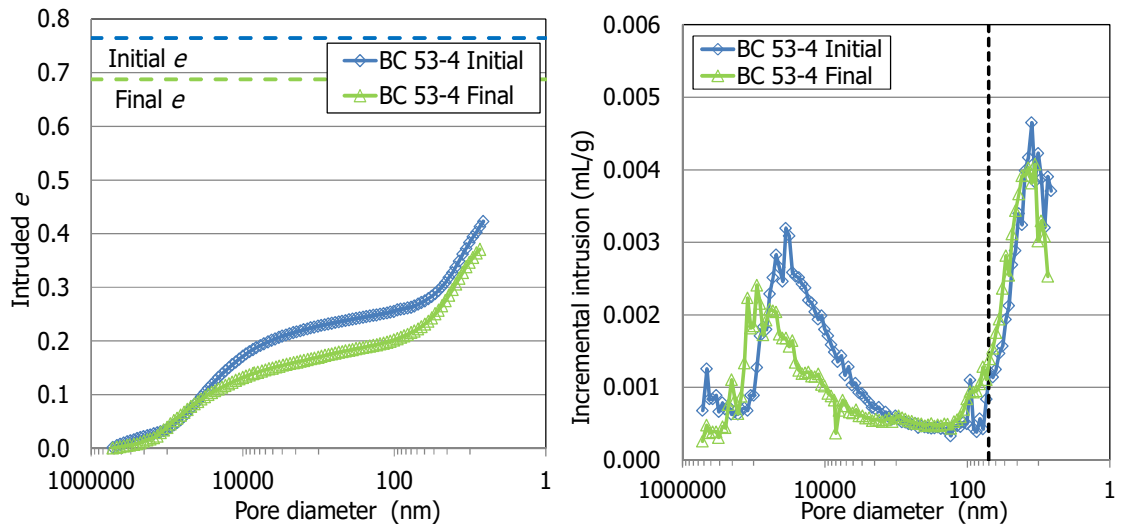
986

987 **Fig. 13: Gas permeability as a function of the accessible porosity for the reference FEBEX bentonite**
 988 **(Eq. 3) and for FEBEX-DP samples with and without interface tested under confining pressures of 0.6**
 989 **and 1.0 MPa (modified from Carbonell et al. 2019)**



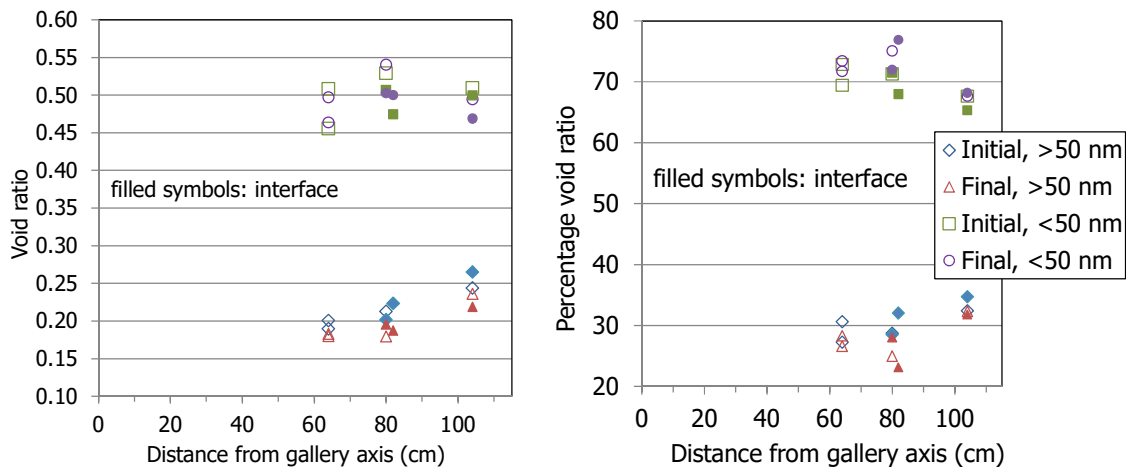
990

991 **Fig. 14: Change in dry density occurred during gas testing as a function of the maximum confining**
 992 **pressure applied during the tests (positive values indicate increase)**



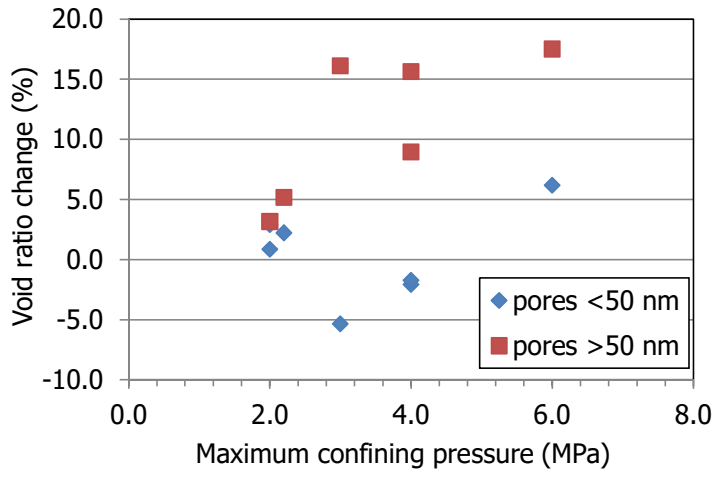
993

994 **Fig. 15: Pore size distribution of sample BC-53-4 ($S_r=96\%$, distance to gallery axis 104 cm, with interface) before**
 995 **and after gas testing (the dotted vertical line indicates de separation between macro and mesopores)**



996

997 **Fig. 16: Void ratio corresponding to pores larger and smaller than 50 nm of the bentonite samples**
 998 **before and after gas testing**



999

1000 **Fig. 17: Change in the void ratio corresponding to pores larger and smaller than 50 nm obtained by**

1001 **MIP after gas testing (positive values indicate decrease)**

1002